Reaction Chemistry & Engineering

ROYAL SOCIETY OF CHEMISTRY

PAPER

View Article Online
View Journal

Check for updates

Cite this: DOI: 10.1039/d6re00015k

Innovative ZSM-5-based catalyst design *via* 3D printing for methanol dehydration to DME

V. Koidi, [ab] S. Koltsakidis,[b] S. Karakoulia,[a] D. Tzetzis,[b] A. A. Lappas[a] and E. Heracleous [*ab]

In the last years, the use of 3D printing for the preparation of structured materials with catalytic functionalities has attracted considerable interest. In this work, using ZSM-5 zeolite as acidity provider, we explore two routes that employ additive manufacturing to prepare structured catalysts for dimethyl ether production *via* methanol dehydration. In the first route, ZSM-5-based monoliths are 3D-printed using crystalline ZSM-5 powder and bentonite clay as a binder. In the second route, α-alumina support structures are first fabricated *via* robocasting, followed by *in situ* hydrothermal synthesis of ZSM-5 on the printed structures. The structured catalysts along with their starting materials are characterized by N_2 adsorption, XRD, pyridine-FTIR, electron microscopy, while stress–strain curves are also obtained to evaluate the monoliths' mechanical stability. The structured catalyst prepared *via* the first route adequately retains the physicochemical properties of the ZSM-5 crystallites. *Via* the second route, ZSM-5 crystallites with good porosity and acidity are grown on the 3D printed α-Al_2O_3 support, achieving a total loading of *ca.* 4 wt%. When compared on an equivalent ZSM-5 basis, the ZSM-5/α-Al_2O_3 catalyst exhibits up to twice the activity in methanol conversion with 100 C-mol% DME selectivity, while it also outperforms the corresponding hydrothermally prepared ZSM-5 powder. This is possibly linked to the excellent dispersion of the ZSM-5 active sites on the 3D-printed α-Al_2O_3 structure, which provides a unique substrate for the growth of surface ZSM-5 nano-crystallites. This work highlights the great potential of employing 3D printing techniques for catalytic applications.

Received 8th January 2026,
Accepted 5th February 2026

DOI: 10.1039/d6re00015k

rsc.li/reaction-engineering

Open Access Article. Published on 12 February 2026. Downloaded on 4/29/2026 9:04:27 PM.
This article is licensed under a Creative Commons Attribution 3.0 Unported Licence.

1. Introduction

Dimethyl ether (DME) is a non-toxic, non-carcinogenic molecule which can be easily liquefied at room temperature under relatively low pressure (≈0.5 MPa) for storage and transportation as a liquid.[1–3] Global demand for DME presents a continuously rising trend due to its multiple uses. Currently, it is mainly used as aerosol propellant in spray cans, as carrier for pesticides, as refrigerant replacement *etc.*[4] It can also be used for the production of alkyl-aromatics, methyl acetate,[5] acetic acid,[6] light olefins[7] and other important compounds, highlighting its potential for the production of chemicals in a future methanol/DME-based economy.[8–10] Apart from its use in the chemical industry, in the last few decades, the concept of using DME as an eco-friendly fuel is receiving growing attention. It does not form explosive peroxides, so it is easy to store and transport, while the existing infrastructure for LPG can be easily modified to handle DME with similar safety guidelines and codes.[11] The lack of C–C bonds and its high oxygen content (35%) lead to decreased emissions of incomplete combustion products (such as CO and unburned hydrocarbons), while its emissions do not contain particulate matter or polluting gases, such as SO_x and NO_x.[1,12–17] The above, combined with its high cetane number, render DME an attractive alternative to the existing transportation fuels, particularly for diesel-fueled applications. Additional applications of DME in the energy sector include its use as a hydrogen carrier due to its comparatively easier handling and high efficiency.

DME is currently produced on commercial scale *via* a two-step process that involves the conversion of natural gas-derived syngas to methanol, and the subsequent dehydration of methanol to DME.[18] The dehydration of methanol to DME (eqn (1)) is an acid-catalyzed exothermic reaction, which typically takes place over γ-Al_2O_3.

$$2CH_3OH \rightleftharpoons CH_3OCH_3 + H_2O \quad \Delta H = -23.4 \text{ kJ mol}^{-1} \qquad (1)$$

Besides γ-Al_2O_3, many other catalytic systems have been studied.[19] Zeolites in particular, have emerged as the most

[a] *Chemical Process & Energy Resources Institute (CPERI), Centre for Research and Technology Hellas (CERTH), 6th km Charilaou-Thermi, Thessaloniki, 57001, Greece. E-mail: eheracle@certh.gr*
[b] *School of Science and Technology, International Hellenic University, 14th km Thessaloniki-Nea Moudania, Thessaloniki, 57001, Greece*

Open Access Article. Published on 12 February 2026. Downloaded on 4/29/2026 9:04:27 PM.
This article is licensed under a Creative Commons Attribution 3.0 Unported Licence.

promising catalysts for the methanol dehydration reaction. Amongst the various zeolites, interest has mainly been directed towards ZSM-5-based catalysts. A main advantage of ZSM-5 compared to γ-Al_2O_3 is its higher resistance to water and its better thermal stability.[20] Moreover, ZSM-5 has acid sites of higher strength than γ-Al_2O_3 and thus presents higher methanol conversion even at relatively low temperatures.[21]

In terms of reactor configuration, the vast majority of commercial DME technologies are based on methanol dehydration in a fixed bed reactor.[22] Packed bed reactors are typically preferred due to their simple design and low maintenance cost that enables efficient operation. However, the non-uniform access of reactants to the catalytic surface can decrease the overall process performance and can cause unexpected hot spots and thermal runaways in the case of exothermic reactions. Another common issue is related to pressure drop. These limitations can be addressed by utilizing structured catalysts with well-defined engineered architectures that can improve reaction rates. Unlike conventional preparation technologies such as extrusion,[23] 3D printing – also known as additive manufacturing – is a bottom-up fabrication method based on the incremental addition of layers of materials. This approach enables the creation of complex and optimized structures in a straightforward, convenient and efficient way. Furthermore, it creates new opportunities for the design and refinement of catalytic structures through computational modeling, thereby improving the mass and heat transfer characteristics of the resulting materials.[24]

The use of 3D printing for complex catalyst manufacturing can result in breakthroughs in the catalysis field. However, its application for the preparation of chemically functional materials is still in early development stage, with a plethora of challenges remaining to be tackled. The primary difficulties are related to the preparation of printing pastes containing the active components,[25–27] which must be both printable and, at the same time, stable at the conditions typically employed in chemical processes. To this end, proper solvents and/or various additives/binders are essential for preparing pastes with the appropriate rheological and physicochemical properties. In most cases, rheological modifiers, such as clays, are introduced to ensure the printability of the inks. These solvents/additives/binders could however have adverse impact on the catalytic performance. Additionally, when post-treatment is necessary, a significant difficulty lies in maintaining both the macroporous and micro/meso structure of the 3D-printed materials.[28] A common problem that occurs when certain extrusion-based printing techniques are employed is that solvent removal can induce shrinkage and pore structure damage.[29] Calcination also negatively affects the pore structure, especially in powder-based printing. The advances in the field of additive manufacturing in catalysis are nicely summarized in several recent reviews.[28,30–34]

Few groups have attempted to prepare catalysts for DME synthesis *via* 3D printing. Lefevere *et al.*[35] prepared 3D-printed zeolites by first manufacturing different stainless-steel structures using three dimensional fibre deposition (3DFD), which were then coated with zeolites following a washcoating procedure. The ZSM-5 coated structures were benchmarked in the conversion of methanol to DME and olefins. Compared to packed bed and honeycomb-type supports, the 3D-printed catalysts demonstrated excellent catalytic properties. High selectivity to DME was achieved at low temperature using a structured catalyst with straight channels, while the structures with tortuous channels exhibited the highest yield to light olefins. Magzoub *et al.*[36] employed additive manufacturing to produce HZSM-5 based structured monoliths. By investigating the monoliths' physicochemical properties and the performance in the methanol-to-DME reaction, they found that the DME selectivity is improved as a result of modifications in the acidity and porosity of the 3D-printed monolith compared to its powder counterpart. In a follow-up work by the same group,[37] doping of HZSM-5 with 4 wt% Ga_2O_3 *via* a direct oxide 3D printing method improved both activity and selectivity, as well as long-term stability in the dehydration reaction. Recently, Bonura *et al.*[38] prepared a 3D-printed catalyst for the direct hydrogenation of CO_2 to DME, using a hybrid CuO–ZnO–ZrO_2/zeolite formulation previously developed by their team diluted with an inorganic silica-based binder. They then compared the structured catalyst's performance with that of the hybrid catalyst in powder form. Though the activity of the 3D-printed catalyst was lower, its overall performance was promising. A correlation was also evidenced between the surface availability of acid–base adsorption sites and catalytic performance. In previous own work,[39] ZSM-5-based zeolite monoliths of woodpile configuration were prepared *via* robocasting, starting from a commercial equilibrium ZSM-5 catalyst powder and bentonite clay as binder. Different zeolite-binder compositions were employed to investigate the effect of binder concentration in the 40–60 wt% range on the rheological, mechanical and physicochemical properties of the structured catalysts. By measuring key properties for catalysis, such as surface area and acidity, we found that the ZSM-5 crystallites retain their porous structure, textural characteristics and largely their acidity during the additive manufacturing process. The structured 3D-printed catalyst with 60 wt% zeolite was thus identified as optimum, demonstrating good physicochemical properties and retaining adequate mechanical strength.

Building on this previous experience, we report in this work the additive manufacturing of improved ZSM-5-based structured catalysts with high acidity and excellent performance in the dehydration of methanol to DME. The catalysts were prepared by robocasting, following different printing strategies: (i) direct fabrication of 3D-printed structured ZSM-5 monoliths using crystalline ZSM-5 powder as starting material, and (ii) fabrication of 3D-printed α-alumina structures, acting as supports for the deposition of ZSM-5 grown *in situ via* hydrothermal synthesis. With this work, we aim to further contribute to the limited literature

This journal is © The Royal Society of Chemistry 2026

Open Access Article. Published on 12 February 2026. Downloaded on 4/29/2026 9:04:27 PM.
This article is licensed under a Creative Commons Attribution 3.0 Unported Licence.

on the application of 3D printing in catalysis by combining innovative synthesis routes for the preparation of structured acidic catalysts, with thorough characterization of their mechanical and physicochemical properties, and evaluation of the methanol-to-DME reaction performance under industrially-relevant operating conditions.

2. Experimental

2.1. Catalyst preparation

Direct manufacturing of ZSM-5-based structures. The procedure followed for the preparation of the direct 3D-printed ZSM-5 monoliths is graphically depicted in Fig. 1a. Commercial crystalline ZSM-5 with SiO_2/Al_2O_3 ratio 23 (Zeolyst) was used as starting material. The zeolite was first calcined at 550 °C for 10 h in air to obtain its protonated form. The ZSM-5 powder was mixed with bentonite clay (Sigma Aldrich) used as binder at a concentration of 60 wt% ZSM-5–40 wt% binder. As stated in the introduction, this composition was found to be optimal based on previous work.[39] Methylcellulose (Sigma Aldrich) was then added to the mixture at a concentration of 1 wt% to promote gelation and shear thinning behavior. Distilled water was added gradually to the solids mixture until saturation to create the printing paste. The resulting paste was directly loaded in the 3D printer to avoid drying that would affect the printability properties. Cylindric monoliths of woodpile configuration with nominal diameter of 12 mm and height of 25 mm were prepared by robocasting on an Engine HR 3D printer (Hyrel 3D) equipped with an EMO printhead. The printing paste was extruded through a 0.6 mm-nozzle with printing speed 8 mm s^{-1} and layer height 0.5 mm. A 50% rectilinear infill was used during slicing, which resulted in nominal pore sizes of 0.66 mm. The monoliths were dried at ambient conditions for 24 h and were then calcined at 500 °C for 5 h in air flow. A total of 10 specimens were printed to provide sufficient statistical estimates. The crystalline ZSM-5 powder and the bentonite clay were also calcined at the same conditions to serve as benchmark. The 3D-printed ZSM-5-containing monoliths are denoted as 3D-C-ZSM-5, while the calcined commercial crystalline ZSM-5 powder is denoted as PWD-C-ZSM-5.

Hydrothermal synthesis of ZSM-5 on α-Al_2O_3 structures. For the manufacture of ZSM-5 on α-Al_2O_3, cylindric α-Al_2O_3 monoliths of woodpile configuration with the same dimensions as those reported above were first prepared by robocasting. To prepare the printing paste, a 20 wt% aqueous solution of Pluronic F-127 powder (Sigma-Aldrich) was first prepared. The solution was left to settle in a refrigerator for 48 h until homogeneity was achieved and was then mixed with 1 wt% on solids of Dolapix CA (Zschimmer & Schwarz), used as dispersant. The printing paste was formed by gradually adding to the solution commercial α-Al_2O_3 (ThermoFisher) with a typical diameter of 0.5–0.7 μm and specific surface area of 3–4 m^2 g^{-1} up to a solid loading of ~40 vol%. The α-Al_2O_3 monoliths were printed on the same

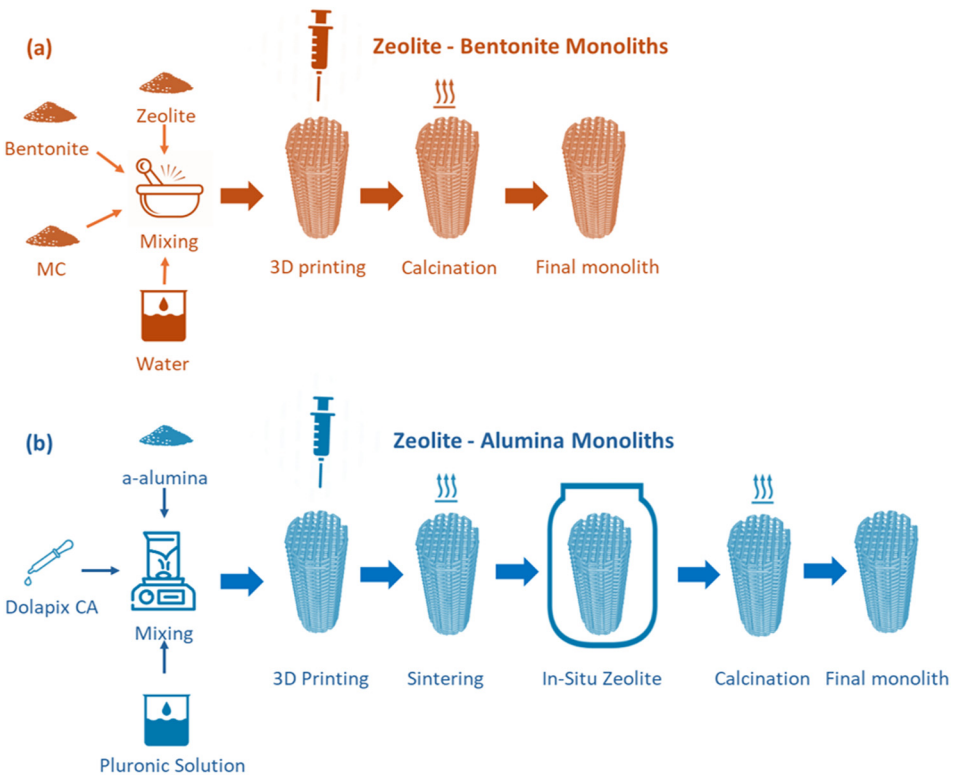

Fig. 1 Preparation sequence for the (a) direct manufacturing of 3D-printed ZSM-5-based monoliths, and (b) hydrothermal synthesis of ZSM-5 on 3D-printed α-Al_2O_3 monoliths.

Open Access Article. Published on 12 February 2026. Downloaded on 4/29/2026 9:04:27 PM.
This article is licensed under a Creative Commons Attribution 3.0 Unported Licence.

3D printer with the same printing parameters as those reported above. The printed monoliths were dried at ambient conditions for 24 h, followed by a 2 h de-binding process at 600 °C and calcination at 1400 °C for 2 h in air. To synthesize the ZSM-5 zeolite (SiO_2/Al_2O_3 ratio 50), a sol solution containing alumina and silica building blocks was first prepared. Tetraethyl orthosilicate (TEOS) served as the silicon source, aluminum nitrate as the aluminum source, and tetrapropylammonium hydroxide (TPAOH, 20 wt% in water) as the organic structure-directing agent. Sodium hydroxide (98% NaOH, pellets) was used to adjust the pH. Initially, the alumina and silica building blocks were prepared separately by stirring their respective precursors in water containing TPAOH for 24 h at room temperature. Subsequently, NaOH was added to the alumina solution until pH reached the value of 10. Then, both solutions were combined and stirred for additional 8 h. The molar composition of the resulting synthesis mixture was: 1 SiO_2 : 0.02 Al_2O_3 : 0.3 TPAOH : 45 H_2O. The 3D-printed α-Al_2O_3 monoliths (5–6 monoliths) were then submerged in the final obtained sol solution and the mixture was transferred to a Teflon-lined autoclave at 170 °C for 5 days without stirring.

The resulting Na-ZSM-5/α-Al_2O_3 monoliths were subjected to ultrasonication to remove the loosely bound Na-ZSM-5 from the monolith's surface. Then washing with distilled water was continued until the pH of the filtrate became neutral. Finally, both the Na-ZSM-5 powder and the Na-ZSM-5/α-Al_2O_3 monoliths underwent ion exchange with 2 M ammonium nitrate at 50 °C for 2 hours using a rotary evaporator as both the bath and stirring medium. The resulting suspension was then filtered and washed until the pH of the filtrate became neutral. The ion-exchanged materials were then calcined in air at 550 °C for 10 h to yield the final products. The entire procedure is depicted schematically in Fig. 1b. The 3D-printed α-Al_2O_3 monoliths are denoted as 3D-Al_2O_3, the ZSM-5/α-Al_2O_3 monoliths as HT-ZSM-5/3D-Al_2O_3 and the hydrothermally synthesized ZSM-5 powder as PWD-HT-ZSM-5.

2.2. Physicochemical properties and morphology

N_2 adsorption/desorption isotherms were obtained at −196 °C with an automated volumetric sorption analyzer (Autosorb-1MP, Quantachrome), after degassing the samples at 250 °C under vacuum overnight, to determine the surface area (BET method), total pore volume at P/P_o = 0.99, micropore volume (*t*-plot method) and pore size distribution (BJH method) of the samples.

Information on the crystalline structure of the materials was obtained by X-ray diffraction (XRD). The measurements were performed on Bruker D8 Advance diffractometer operated at 40 kV and 30 mA with Cu Kα radiation (=0.154 nm). Diffractograms were recorded in the 5–80° (2θ) range with a step size of 0.05° and at a scanning rate of 0.01° s^{-1}. Quantitative phase analysis *via* Rietveld refinement was performed to determine the relative amount of zeolite in the HT-ZSM-5/3D-Al_2O_3 monolith using the Profex/BGMN software. For the α-Al_2O_3 phase, the standard structure file provided in the internal Profex–BGMN structure database (.str format) was employed. The ZSM-5 phase was introduced from the crystallographic information file (.cif format) reported by Schmidt *et al.*[40] and obtained from the Crystallography Open Database (COD, entry 1 505 106), after appropriate compatibility conversion to a BGMN-compatible .str file.

The Na and K content of bentonite and the Na and Al content of the commercial and synthetic zeolitic powders were measured by inductively coupled plasma-atomic emission spectroscopy (ICP-AES) on a spectrophotometer Optima 4300 DV (PerkinElmer). The C content in the used samples was determined *via* the CS400 system. This method specifically analyzes carbon and sulfur by combusting the sample in an oxygen-rich environment and measuring the emitted gases using infrared detectors offering high sensitivity for low concentrations.

The acidic properties of the materials were determined with *in situ* FT-IR after pyridine adsorption using a Nicolet 5700 FT-IR spectrometer (resolution 4 cm^{-1}) equipped with a homemade stainless-steel IR cell with CaF_2 windows by means of the OMNIC software. Self-supporting wafers (~15 mg cm^{-2}) were loaded in the infrared cell, which is connected to a high vacuum line consisting of turbomolecular and diaphragm pumps. Detailed description of the followed procedure can be found in previous work.[39] The calculation of the acid sites was based on the integrated Lambert–Beer law, while the Brønsted (band at ~1540 cm^{-1} attributed to pyridinium ions) and Lewis (band at ~1445 cm^{-1} attributed to coordinated pyridine) molar extinction coefficients of Emeis were employed.[41]

The monoliths' homogeneity and structure adhesion were evaluated by Scanning Electron Microscopy (SEM) on a Phenom ProX Microscope (ThermoFisher Scientific). The samples were gold-coated using an ion sputtering device (Quorum SC7620) and were mounted onto double adhesive conductive carbon tabs (TED Pella) on an aluminum stub to be scanned at an accelerating voltage of 10 kV.

It should be noted that for all the above characterization methods – apart from SEM – the structured catalysts were first crushed to powder form.

2.3. Mechanical properties

Compression experiments were conducted using a universal testing machine (Model M500-50AT, Testometric) at a constant crosshead speed of 1 mm min^{-1}. The machine was equipped with a 0.01 newton resolution load cell. The compressive stress of the monoliths was calculated by dividing the recorded compressive force by the cross-sectional. Compressive strength was defined as the maximum compressive stress. Each test was repeated three times to ensure reliable statistical data.

This journal is © The Royal Society of Chemistry 2026

Open Access Article. Published on 12 February 2026. Downloaded on 4/29/2026 9:04:27 PM.
This article is licensed under a Creative Commons Attribution 3.0 Unported Licence.

2.4. Catalytic performance evaluation

The catalytic performance in the methanol dehydration reaction was assessed in a continuous high-pressure dual fixed-bed reactor unit (Microactivity Effi-PID). The unit's feeding system consists of three gas lines, each equipped with high accuracy mass flow controllers, and one liquid feed line, using a high precision pump. The liquid feed system also includes a pressurized storage vessel which contains the liquid to be pumped. The stainless-steel fixed bed reactors (ID: 9.1 mm) are placed in furnaces made by ceramic fibers which house the heating resistors. The reaction temperature is monitored with a thermocouple inserted in the catalyst bed. All components that comprise the equipment are housed inside a hot box at a temperature of up to 200 °C to prevent condensation. The exit stream of the reactors is sent to liquid–gas separators for separation and collection of the liquid and gaseous products. The volumetric flow of the gaseous exit stream is measured *via* a mass flow meter (MFM).

In a typical experiment, the required number of monoliths was introduced into the reactor to attain the targeted ZSM-5 amount in the catalytic bed. Experiments with the benchmark commercial and hydrothermally synthesized ZSM-5 powders were also conducted. The powder samples were first sieved to obtain particle sizes in the 90 μm $< d <$ 150 μm range and then diluted with inert SiC (particle size ≈ 210 μm) at a ZSM-5 : SiC mass ratio of 1 : 3 to ensure uniform temperature distribution and avoid local hot-spots. It should be noted that the total bed volume of the powder samples was smaller than that of the structured catalysts.

The materials were first pre-treated by heating at the reaction temperature with a rate of 5 °C min^{-1} for 0.5 h under N_2 flow. The experiments were conducted at a temperature range of 225–275 °C and a WHSV range of 5–70 h^{-1} calculated on ZSM-5 basis, with constant pressure equal to 10 bar and 50 vol% CH_3OH in N_2 feed. N_2 was fed in the reactor in the gas form, while methanol was introduced in liquid form *via* the HPLC pump. Steady-state activity data were obtained after 1 h of time-on-stream. The liquid and gaseous products were analyzed with a GC 7890 gas chromatograph (Agilent Technologies) equipped with a dual FID/TCD detector. The H_2O concentration in the liquid product was determined by Karl-Fischer titration according to ASTM E203-08. Mass and carbon balances typically closed to within ±5%. The N_2 used was of purity above 99.999% and methanol ≥99.9% (Chromasolv™, HPLC Honeywell Riedel-de Haën™). The reaction performance was evaluated on the basis of methanol conversion and DME selectivity on carbon-molar basis, calculated as shown below:

$$\text{Conversion } CH_3OH\ (\%) = 100 \times \left(1 - \frac{n_{CH_3OH,out}}{n_{CH_3OH,in}}\right) \quad (2)$$

$$\text{Selectivity DME}\ (\%) = 100 \times \left(\frac{2n_{DME,out}}{n_{CH_3OH,in} - n_{CH_3OH,out}}\right) \quad (3)$$

where n_{in}, n_{out} stand for the molar flow of each compound in the inlet and outlet of the reactor, respectively.

3. Results & discussion

3.1. Characterization results

Direct 3D-printed ZSM-5 structures. The ZSM-5-containing 3D-printed monoliths were first visually inspected with SEM to assess their morphology. The obtained images, shown in Fig. 2a and b, demonstrate a uniform distribution and good dispersion of the ZSM-5 particles within the bentonite matrix at microstructure level. However, on a macroscopic level (Fig. 2a), the struts of the monolith are not very well defined.

The textural properties of the commercial crystalline ZSM-5 powder, the bentonite binder and the direct 3D-printed ZSM-5 monolith were determined *via* N_2 adsorption/desorption and are presented in Table 1. The corresponding N_2 adsorption/desorption isotherms and the Barrett–Joyner–Halenda (BJH) pore-size distributions are shown in Fig. 3a and b, respectively.

The crystalline ZSM-5 powder presents a type I isotherm typical of microporous materials,[42] accompanied by a flat H4

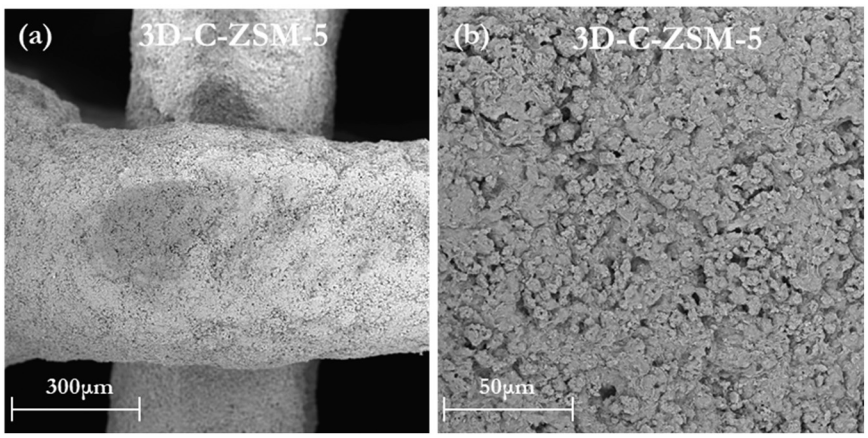

Fig. 2 SEM images of the (a) struts and (b) microstructure of the direct 3D-printed ZSM-5 monolith.

Open Access Article. Published on 12 February 2026. Downloaded on 4/29/2026 9:04:27 PM.
This article is licensed under a Creative Commons Attribution 3.0 Unported Licence.

Table 1 Textural properties of the direct 3D-printed ZSM-5 monolith and starting materials

	Surface area, $m^2\ g^{-1}$		Pore volume, $cm^3\ g^{-1}$			
Sample	BET[a]	Micropore[b]	Micropore	Meso-macropore	Textural[c]	Total[d]
PWD-C-ZSM-5	402	318	0.122	0.064	0.059	0.245
Bentonite	29	0	0.000	0.043	0.063	0.106
3D-C-ZSM-5	265	203	0.078	0.059	0.048	0.185

[a] From multi-point BET method. [b] From *V*–*t* analysis plot method. [c] Textural volume = total pore volume − volume calculated at P/P_o = 0.90. [d] Calculated at P/P_o = 0.99.

hysteresis loop. The microporous structure of the crystalline ZSM-5 powder is also corroborated by the determination of the micropore surface area and volume *via* *t*-plot analysis (Table 1). The 3D-printed monolith exhibits an isotherm of similar type, but with a more pronounced hysteresis loop. This can be attributed to the contribution of the bentonite binder, which has larger pores and low surface area, and thus leads to the enhancement of mesoporosity and the formation of significantly larger pores.[43] Moreover, the increase of the adsorbed nitrogen volume in the monolith at high relative pressure indicates an important external surface area contribution. The BJH pore size distribution curves of the ZSM-5 powder and the monoliths demonstrate a well-defined peak at 30–40 Å. This feature does not represent real pores, but it is rather caused by a transition of the adsorbed phase from a lattice fluid-like phase to a crystalline-like solid phase, typical for ZSM-5 zeolites.[44]

The BET surface area and the micropore volume of the 3D-printed monolith is very close to the nominal values calculated based on the corresponding properties of crystalline ZSM-5 and bentonite at the specific concentration. These promising findings clearly demonstrate that the ZSM-5 crystals retain their porous structure and textural characteristics and are not affected by the additive manufacturing process. The above agrees with Lefevere *et al.*[45] who also prepared structured ZSM-5-based catalysts *via* 3D printing using bentonite as binder and observed no significant differences between the textural properties of the

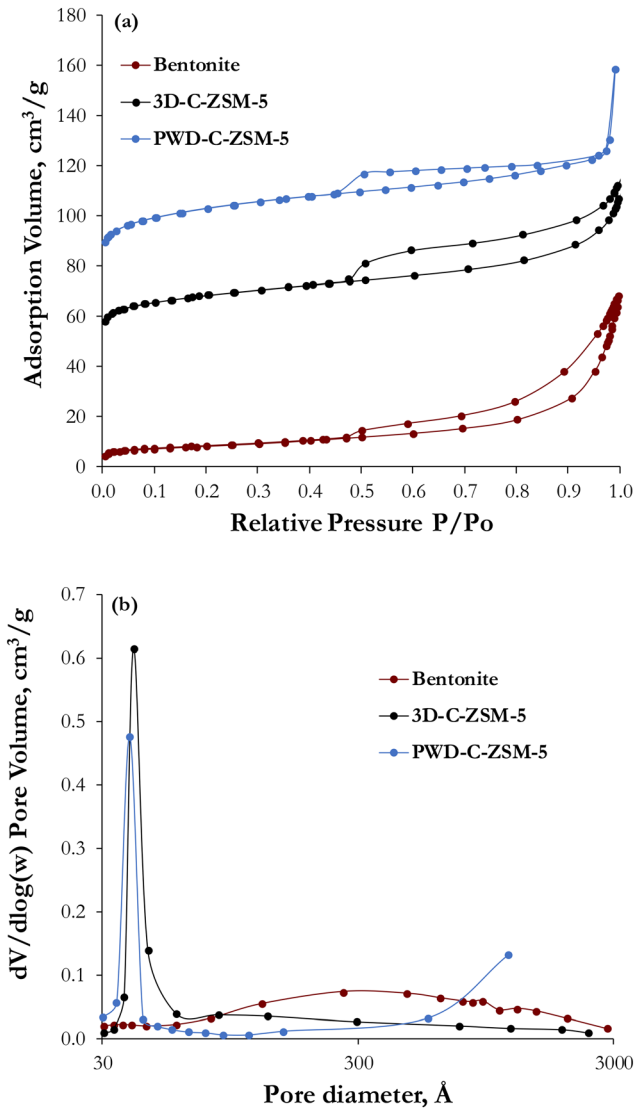

Fig. 3 (a) N_2 adsorption/desorption isotherms and (b) BJH pore size distribution of the direct 3D-printed ZSM-5 monolith and starting materials.

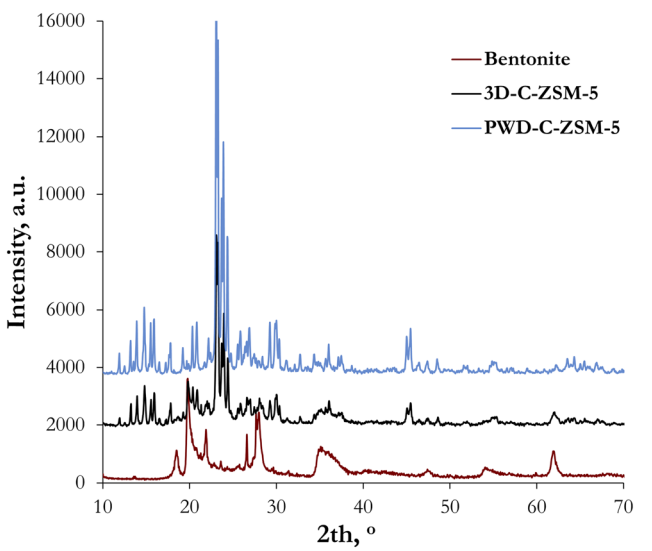

Fig. 4 XRD patterns of the direct 3D-printed ZSM-5 monolith and starting materials.

This journal is © The Royal Society of Chemistry 2026

Open Access Article. Published on 12 February 2026. Downloaded on 4/29/2026 9:04:27 PM.
This article is licensed under a Creative Commons Attribution 3.0 Unported Licence.

monoliths relative to the percentage of ZSM-5 zeolite loaded into the structure.

This is also confirmed by the XRD patterns presented in Fig. 4 for the monolith and its starting materials. The well-defined crystalline structure of zeolite ZSM-5 (JCPDS 44-0003) is retained in the monolith as well. The diffraction peaks exhibit comparable sharpness to their powder form with slightly reduced intensity, which can be attributed to the lower zeolite content in the monolith. The additional diffractions at 21.9°, 27.8°, 35.6°, 54.1°, and 61.9° in the diffractograms of the structured samples are characteristic of the bentonite binder crystalline structure (JCPDS 003-0019).

Acidity is a key property for the catalytic performance of the 3D-printed ZSM-5 monoliths, as methanol dehydration to DME is an acid-catalyzed reaction. Chemisorption of pyridine, followed by *in situ* FT-IR, was employed to detect the number and strength of Lewis and Brønsted acid sites. The total acidity, the number and strength of Brønsted and Lewis acid sites, as well as the Brønsted/Lewis ratio (B/L), are shown in Fig. 5. The crystalline ZSM-5 powder presents, as expected, the highest acidity, mainly of Brønsted type (B/L = 4.0) and high strength, attributed to the bridging framework hydroxyls of ZSM-5.[46] The 3D-printed monolith exhibits considerably reduced acidity and lower B/L ratio. The reduction is greater than that expected based solely on the binder dilution effect, as shown clearly by the acidity values expressed both on total monolith and on ZSM-5 basis in Fig. 5. This result suggests that the printing procedure has an adverse impact on the acidic properties of ZSM-5. Lefevere *et al.*[45,47] also observed a decrease in the number of acid sites, both per surface and per weight, of a structured ZSM-5/bentonite catalyst compared to the pure zeolite powder. They related this decrease to the existence of sodium in the binder and its adsorption on the acid sites of ZSM-5. Magzoub *et al.*[36] supported that the differences in acidity between an H-ZSM-5-based monolith and its corresponding powder could either be attributed to the addition of the binder and/or to possible sintering between the zeolite particles, thus reducing some of the site accessibility. Vishwanathan *et al.*[21] reported that the deposition of sodium on the surface of ZSM-5 reduced its surface acidity mainly by eliminating strong acid sites. Borade *et al.*,[48] who studied the effect of sodium poisoning on acid sites in ZSM-22 zeolites, showed that introduction of sodium into zeolites, even at a very low level, poisons both strong and weak Brønsted acid sites, with the rate of poisoning being higher for the strong Brønsted sites. They also showed that the surface Brønsted acid sites are preferentially poisoned compared to those inside the zeolite matrix. Baba *et al.*[49] reviewed the literature on the poisoning of acid sites by Na^+ and K^+ ions and showed that these cations have a strong effect on the acidic OH^- groups. They showed that K^+ ions are a more effective poison than Na^+ ions. Makshina *et al.*[50] studied the effect of modification of ZSM-5 catalysts with K and showed that it causes a strong decrease of Brønsted acid sites, while the Lewis acid sites are mostly affected in terms of strength.

Prompted by the above, the Na and K content of the bentonite binder employed for the preparation of the direct 3D-printed monoliths was determined *via* ICP-AES. The Na content was found to be equal to 1.57 wt% and the K content 0.3 wt%. Therefore, the extensive reduction of the strong Brønsted acid sites in the 3D-printed ZSM-5 monolith and the decrease in the B/L ratio could be partially attributed to the basic cations in bentonite and to lower exposure of ZSM-5 on the surface of the monolith due to the embedding of the ZSM-5 particles within the bentonite matrix. Still, the structured ZSM-5 material preserves a significant number of acid sites, which as will be shown later, provides adequate performance in methanol dehydration to DME.

***In situ* grown ZSM-5 on α-Al_2O_3 3D-printed structures.** In the second preparation route explored in this study, α-alumina monolithic structures were first prepared *via* direct 3D printing and were calcined at high temperature (1400 °C) with the aim to minimize internal porosity and achieve improved mechanical properties. The surface morphology of the sintered ceramic α-Al_2O_3 monoliths is illustrated in Fig. 6, showing clearly a uniform and robust morphology without any cavities or cracks. The ZSM-5/α-Al_2O_3 monoliths, formed by the *in situ* hydrothermal growth of ZSM-5 crystals on the support, were also analyzed with SEM. Fig. 7 presents SEM images highlighting the structural and surface characteristics of the ZSM-5/α-Al_2O_3 monoliths. In the depicted image, well-defined ZSM-5 crystals are clearly visible on the surface of the struts, indicating successful *in situ* crystallization during the synthesis process. The surface morphology also suggests strong integration of the zeolite phase within the alumina matrix. To confirm the formation of ZSM-5 crystals on the alumina substrate, EDX analysis was

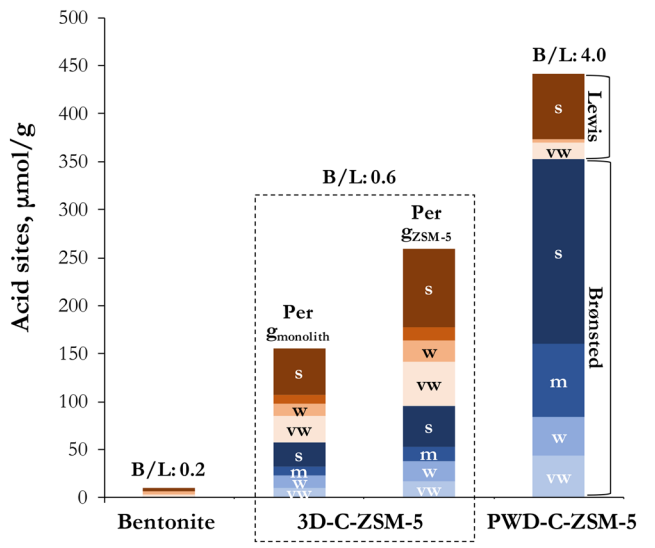

Fig. 5 Acidic properties of the direct 3D-printed ZSM-5 monolith and starting materials (type of sites: Brønsted (blue), Lewis (red), strength of sites: strong (s), medium (m), weak (w) and very weak (vw)). The values on top of the bars refer to the Brønsted-to-Lewis acid sites ratio.

Open Access Article. Published on 12 February 2026. Downloaded on 4/29/2026 9:04:27 PM.
This article is licensed under a Creative Commons Attribution 3.0 Unported Licence.

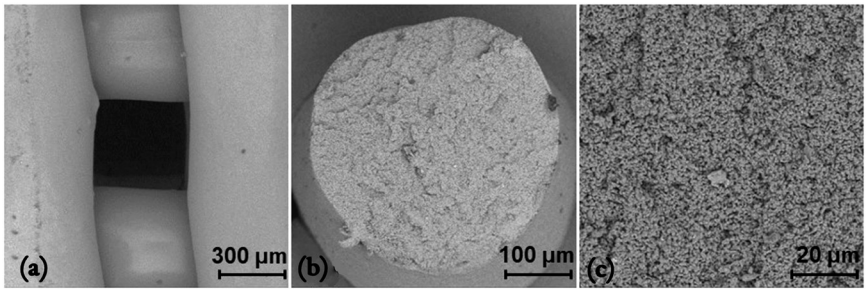

Fig. 6 SEM images of the α-Al_2O_3 3D-printed monoliths captured at various magnifications depict the following aspects: (a) macro-porosity and architecture, (b) cross-sectional views of the filaments, (c) examination of the microstructure within filaments' cross-sections.

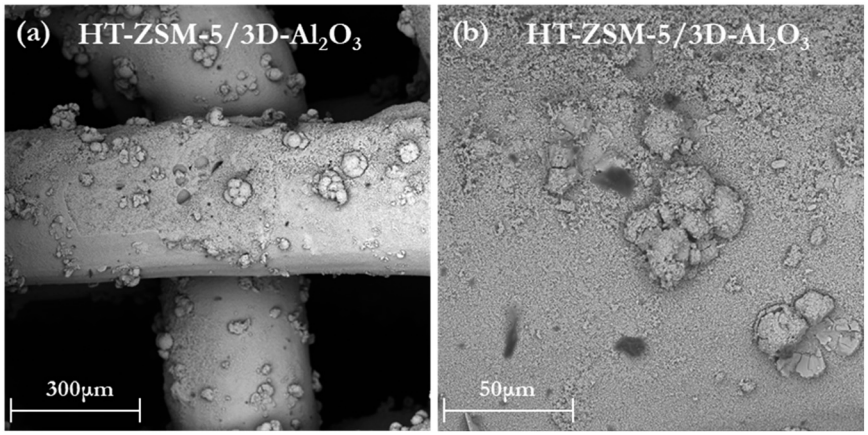

Fig. 7 SEM images of the (a) struts of the ZSM-5/α-Al_2O_3 3D-printed monoliths, displaying successful formation of ZSM-5 crystals on the surface and (b) close-up view of the ZSM-5 crystals on the surface.

performed. Fig. 8a shows the SEM micrograph indicating the specific area where the elemental analysis was performed. Fig. 8b displays the corresponding EDX spectrum, identifying the characteristic peaks of the elements present. In Fig. 8c, a combined elemental map reveals regions with high silicon concentration, highlighted in yellow, indicating the presence of zeolite crystals. Fig. 8d shows the distribution of alumina across the analyzed area, while Fig. 8e and f map the spatial distribution of silicate and sodium, respectively. Together, these results confirm the successful incorporation and surface localization of key elements associated with ZSM-5 formation.

In addition, compression tests were performed on the ZSM-5/α-Al_2O_3 3D-printed monoliths to confirm the expected high mechanical strength. The same tests were also performed on the direct 3D-printed ZSM-5 monolith for comparison reasons. The derived stress–strain curves are presented in Fig. 9. The data shows that both materials reach their peak stress at approximately 6% strain. However, the alumina monolith demonstrates significantly higher compressive strength of 2.9 MPa, compared to just 0.92 MPa for the ZSM-5/bentonite monolith. This disparity is attributed to differences in their internal structures: alumina, being a dense sintered ceramic, can withstand much greater compressive forces, whereas bentonite contains dispersed zeolite in its matrix, making it structurally weaker and more prone to failure. The zigzag pattern observed in the alumina curve is characteristic of ceramic materials and reflects the formation of small strut cracks leading up to the critical failure point and the subsequent sharp drop in load. In contrast, the bentonite monolith exhibits a smoother curve, indicating its tendency to disintegrate rather than crack in a stepwise fashion.

Table 2 presents the textural properties of the α-Al_2O_3 3D-printed monoliths, the ZSM-5 powder that was *in situ* synthesized hydrothermally and the resulting ZSM-5/α-Al_2O_3 monoliths. In addition, ICP-AES analysis showed that the calcined hydrothermally synthesized ZSM-5 powder contains 2.1 wt% Al and 0.7233 wt% Na. Further ion-exchange steps to minimize the Na content were not undertaken to avoid any potential collapse of the 3D-printed structure due to the relatively severe experimental conditions that would be required (stirring for 2 h at 50 °C). The corresponding N_2 adsorption/desorption isotherms and the Barrett–Joyner–Halenda (BJH) pore-size distribution are shown in Fig. 10a and b, respectively. The adsorption isotherm of the *in situ* synthesized ZSM-5 powder is typical for microporous materials (type I in the IUPAC classification),[42] also exhibiting the typical porosity characteristics of a zeolite of MFI type, confirming its successful synthesis. The microporous

This journal is © The Royal Society of Chemistry 2026

Open Access Article. Published on 12 February 2026. Downloaded on 4/29/2026 9:04:27 PM.
This article is licensed under a Creative Commons Attribution 3.0 Unported Licence.

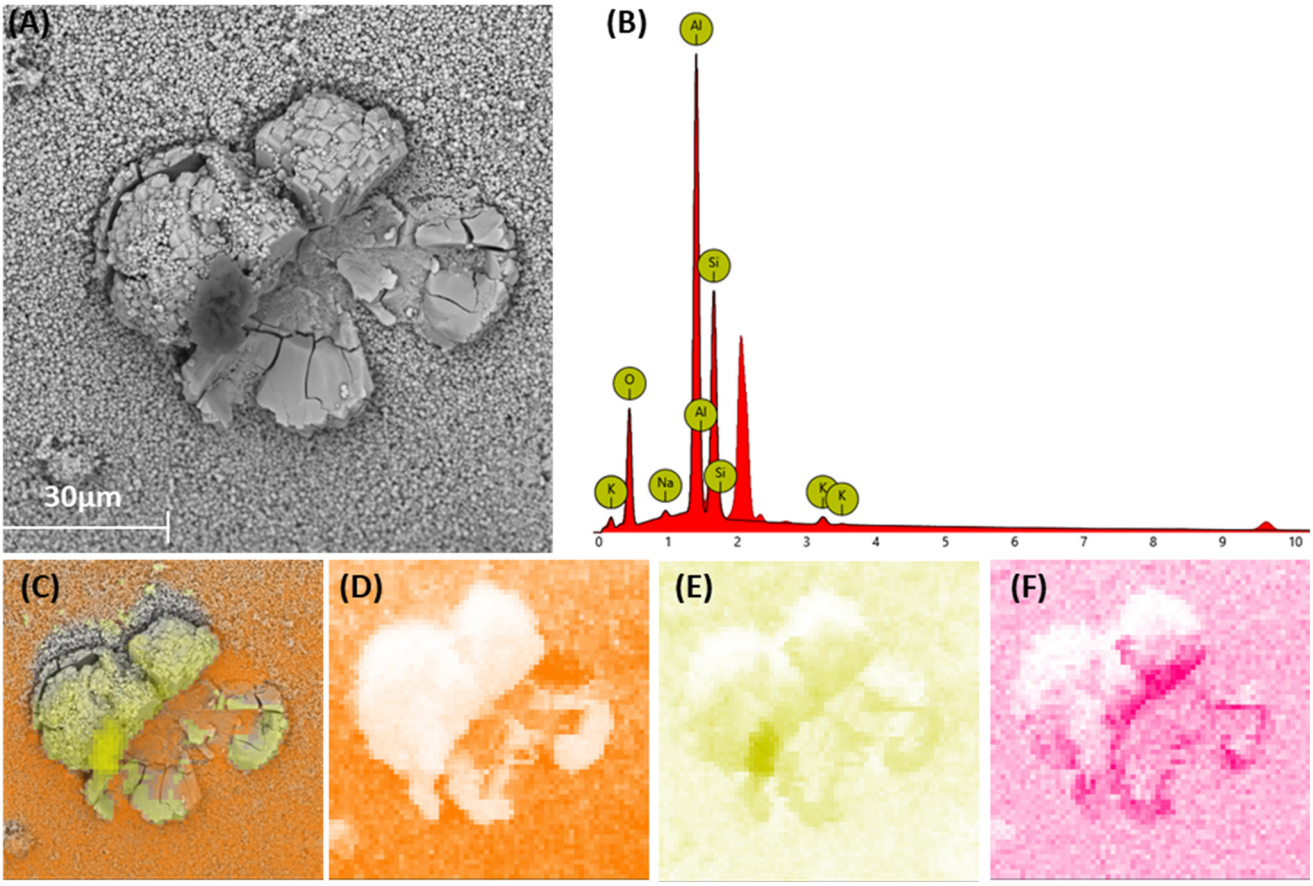

Fig. 8 EDX analysis performed on the surface of the ZSM-5/α-Al_2O_3 3D-printed monoliths: (A) SEM image showing the area of analysis, (B) elemental peak identification, (C) combined element mapping highlighting regions of high Si concentration (yellow area), (D) alumina pixel identification, (E) silicate pixel identification, and (F) Na pixel identification.

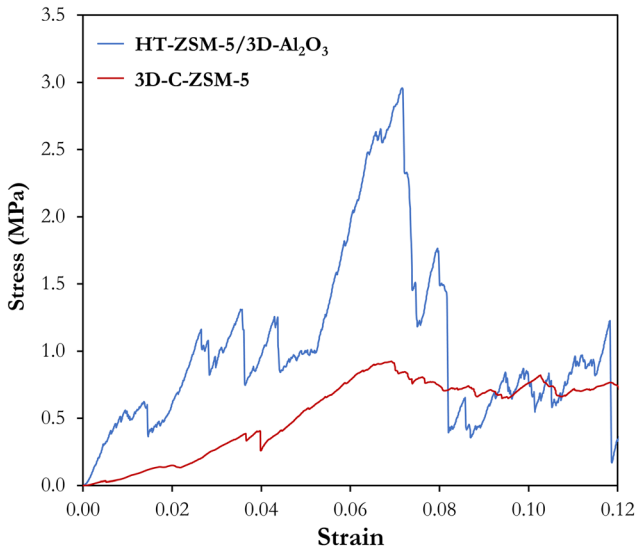

Fig. 9 Stress–strain diagram derived from compression tests on the 3D-printed ZSM-5/α-Al_2O_3 and the direct 3D-printed ZSM-5 monoliths.

structure of the *in situ* synthesized ZSM-5 powder is also corroborated by *t*-plot analysis, as shown in Table 2. The 3D-printed α-Al_2O_3 monolith exhibits on the other hand a type II isotherm, indicative of non-porous materials.[42] The ZSM-5/α-Al_2O_3 monolith presents a similar type II isotherm, with slightly higher adsorption volume over the whole range of relative pressures compared to the α-alumina substrate. This increase could be attributed to the growth of the micro-porous ZSM-5 zeolite on the surface of the substrate. Regarding the BJH pore size distribution, as with the rest of the ZSM-5-based materials examined, there is a well-defined peak around 3–4 nm, which does not represent real pores but is typical of ZSM-5 zeolites.[44] This peak only appears in the ZSM-5 containing samples, thus indicating successful ZSM-5 crystallization on α-alumina. The considerably lower intensity of this peak in the ZSM-5/α-Al_2O_3 monolith can be related to the low concentration of the crystalline ZSM-5 hydrothermally grown *in situ* on the monolith. The above can also be deduced by comparing the measured BET surface areas and pore properties of the three materials (Table 2). Assuming linear contribution of the bare α-Al_2O_3 monolith and the ZSM-5 powder to the surface area and porosity of the ZSM-5/α-Al_2O_3 monolith, simple mathematical calculations suggest a ZSM-5 loading on the monolith of 3.5 wt% based on surface area and 4.4 wt% based on total pore volume.

Open Access Article. Published on 12 February 2026. Downloaded on 4/29/2026 9:04:27 PM.
This article is licensed under a Creative Commons Attribution 3.0 Unported Licence.

Table 2 Textural properties of the hydrothermally synthesized ZSM-5 powder and the 3D-printed α-Al_2O_3 and ZSM-5/α-Al_2O_3 monoliths

	Surface area, $m^2\ g^{-1}$		Pore volume, $cm^3\ g^{-1}$			
Sample	BET[a]	Micropore[b]	Micropore	Meso-macropore	Textural[c]	Total[d]
PWD-HT-ZSM-5	399	283	0.110	0.069	0.008	0.187
3D-Al_2O_3	2	0	0.000	0.002	0.004	0.006
HT-ZSM-5/3D-Al_2O_3	16	9	0.004	0.005	0.005	0.014

[a] From multi-point BET method. [b] From *V*–*t* analysis plot method. [c] Textural volume = total pore volume − volume calculated at P/P_o = 0.90. [d] Calculated at P/P_o = 0.99.

The diffractograms obtained *via* XRD and shown in Fig. 11a corroborate the above. The ZSM-5/α-Al_2O_3 monolith mainly presents diffractions of similar sharpness and intensity as the α-Al_2O_3 monolith that are ascribed to the α-alumina structure (JCPDS 046-1212). It also exhibits peaks characteristic of the ZSM-5 crystalline structure (JCPDS 44-0003). This is shown more clearly in the inset of Fig. 11a that zooms in the 2θ range from 10–25°. In the inset, the signal of HT-ZSM-5/3D-Al_2O_3 has been multiplied ×10 to observe the common peaks between the HT-ZSM-5 powder and the ZSM-5/α-Al_2O_3 monolith. Quantitative phase analysis *via* Rietveld

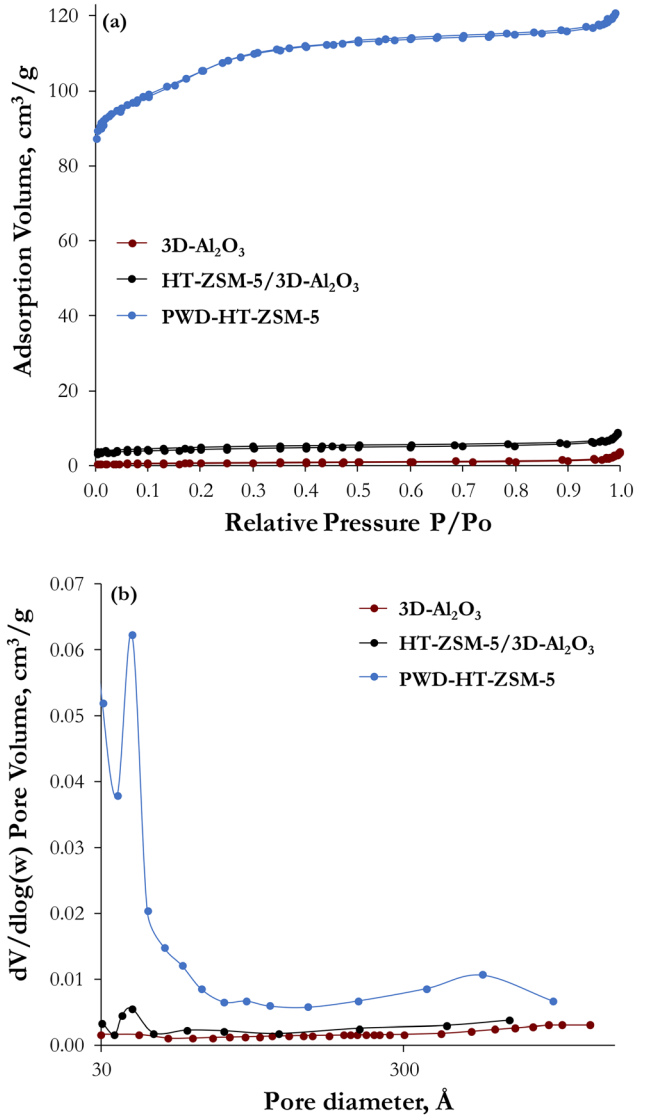

Fig. 10 (a) N_2 adsorption/desorption isotherms and (b) BJH pore size distribution of the hydrothermally synthesized ZSM-5 powder and the 3D-printed α-Al_2O_3 and ZSM-5/α-Al_2O_3 monoliths.

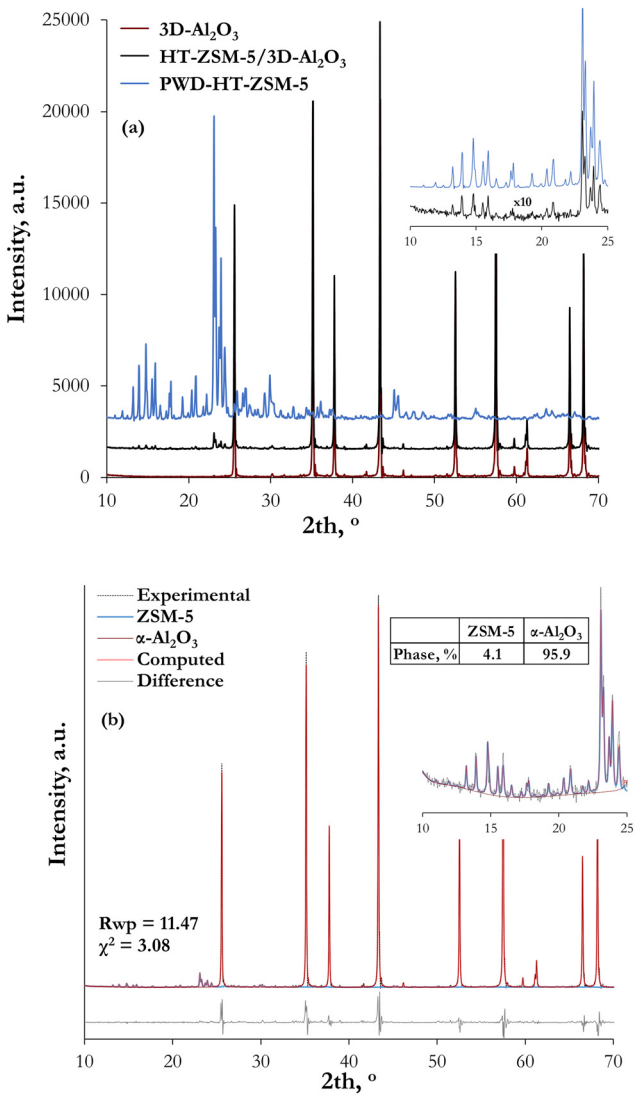

Fig. 11 (a) XRD patterns of the hydrothermally synthesized ZSM-5 powder and the 3D-printed α-Al_2O_3 and ZSM-5/α-Al_2O_3 monoliths and (b) Rietveld refinement of the ZSM-5/α-Al_2O_3 monolith. Insets show magnified views of the 10–25° 2th region.

This journal is © The Royal Society of Chemistry 2026

Open Access Article. Published on 12 February 2026. Downloaded on 4/29/2026 9:04:27 PM.
This article is licensed under a Creative Commons Attribution 3.0 Unported Licence.

refinement was performed to assess the ZSM-5 loading on the monolith. The Rietveld refinement fit, illustrated in Fig. 11b, shows good agreement between the experimental and calculated intensities. The good quality of the fit is also evidenced by the statistical parameters (R_{wp} = 11.47%, χ^2 = 3.08) and the residuals that do not point out to any systematic misfit. Based on the structural refinement, the ZSM-5 loading on the monolith is 4.1% (± 0.16%), a value close to those estimated on the basis of the surface area and porosity of the sample. It should be noted that no explicit corrections for microabsorption or preferred-orientation were applied for the fitting and are thus not accounted for in the calculated uncertainty. Considering the consistency between the three independent approaches followed for ZSM-5 loading estimation, as well as the statistical uncertainty of Rietveld refinement, an average of ~4 wt% is adopted hereafter.

The acidity of the materials was determined by FTIR-pyridine analysis and the results are presented in Fig. 12. Chemisorption of pyridine followed by IR does not detect any acid sites on the 3D-printed α-alumina substrate. On the contrary, the *in situ* synthesized HT-ZSM-5 powder possesses plenty of acid sites, with the majority being of Brønsted type (B/L = 2.6) with high strength. Compared to the commercial ZSM-5 used for the preparation of the 3D-C-ZSM-5 monolith (see Fig. 5), its acidity and B/L ratio are lower which is attributed (as expected) to its higher SiO_2/Al_2O_3 ratio. The ZSM-5/α-Al_2O_3 monolith only demonstrates a very small number of both Lewis and Brønsted acid sites. This is consistent with the low ZSM-5 amount (4 wt%) estimated to have grown on the alumina substrate, based on structural refinement *via* Rietveld analysis and its textural properties. When its acidity is however expressed on ZSM-5 basis, the normalized total number of acid sites is remarkably similar to that of the ZSM-5 powder, suggesting an excellent dispersion of the acid sites on the α-Al_2O_3 substrate. Only modest differences are observed in the type and strength of the acid sites, with a slight increase in Lewis acidity at the expense of Brønsted acidity in the monolith, along with a slight weakening of both Brønsted and Lewis sites. The growth of the ZSM-5 crystallites on α-Al_2O_3 may cause small defects/distortion to the framework Al species and/or formation of extra-framework octahedrally coordinated Al species that both act as Lewis acid centers.[51]

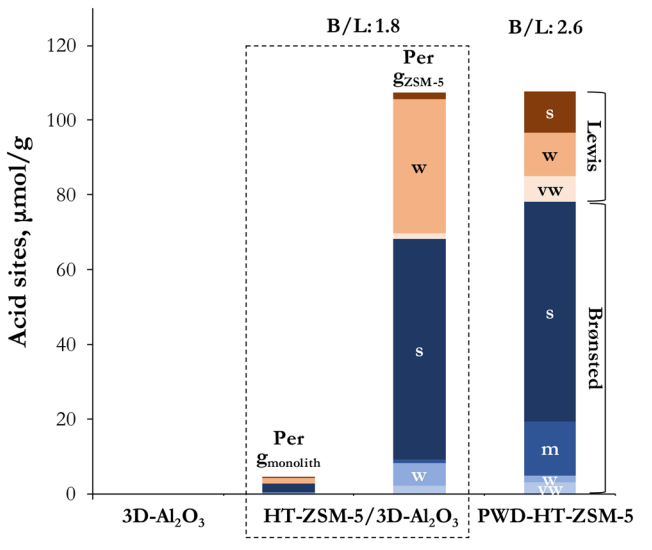

Fig. 12 Acidic properties of the hydrothermally synthesized ZSM-5 powder and the 3D-printed α-Al_2O_3 and ZSM-5/α-Al_2O_3 monoliths (type of sites: Brønsted (blue), Lewis (red), strength of sites: strong (s), medium (m), weak (w) and very weak (vw)). The values on top of the bars refer to the Brønsted-to-Lewis acid sites ratio.

3.2. Catalytic performance in the methanol-to-DME reaction

The catalytic performance of the ZSM-5-containing 3D-printed monoliths, manufactured *via* two different preparation strategies, was assessed in the methanol dehydration reaction to DME in a continuous operation high-pressure setup equipped with a fixed-bed reactor. Based on the findings of our previous work that included the study of the effect of the drying and calcination process on the printed monoliths' dimensions,[39] the monoliths prepared herein were designed to fit in the reactor of the unit depicted in Fig. 13 (monolith dimensions after calcination: 9 mm diameter and 20 mm height). To achieve the desired catalyst loading, multiple specimens were stacked in the reactor.

Methanol dehydration to DME is an exothermic, equimolar reaction (eqn (1)) and thus, DME formation is thermodynamically favored at low temperatures with no major pressure effect. The reaction can be carried out in both the vapor and liquid phase at moderate pressures up to 20 bar, and in the temperature range 100–300 °C.[20] The optimum conditions depend strongly on the employed catalyst.[52,53] ZSM-5, due to its high acidity, offers high activity at relatively low temperatures.[20] Herein, the catalytic performance of the 3D-printed monoliths was evaluated using 50 vol% CH_3OH in N_2 as feed at pressure 10 bar, temperature between 225–275 °C and WHSV in the range of 5–70 h^{-1} calculated on ZSM-5 basis. The commercial crystalline and *in situ* synthesized ZSM-5 powders were also tested for comparison. Calculation of commonly used criteria to determine internal/external mass and heat transfer limitations, such as the Carberry, the Weisz–Prater, the Mears and the Anderson criteria (see SI), do not indicate dominant transport limitations under the employed operating conditions and applied assumptions, suggesting that the observed reaction performance can be attributed primarily to intrinsic catalytic effects. Under all conditions and with all tested materials, the major carbon-containing product was DME, with a carbon-based selectivity of >99.5 C-mol%. Negligible amounts of by-products (*i.e.* isobutane, isopentane, ethanol, ethane, ethylene, propylene) were detected only in the case of the ZSM-5 powder samples at reaction temperature ≥250 °C. Therefore, only CH_3OH conversion is presented as a measure of the materials' performance in the reaction.

Open Access Article. Published on 12 February 2026. Downloaded on 4/29/2026 9:04:27 PM.
This article is licensed under a Creative Commons Attribution 3.0 Unported Licence.

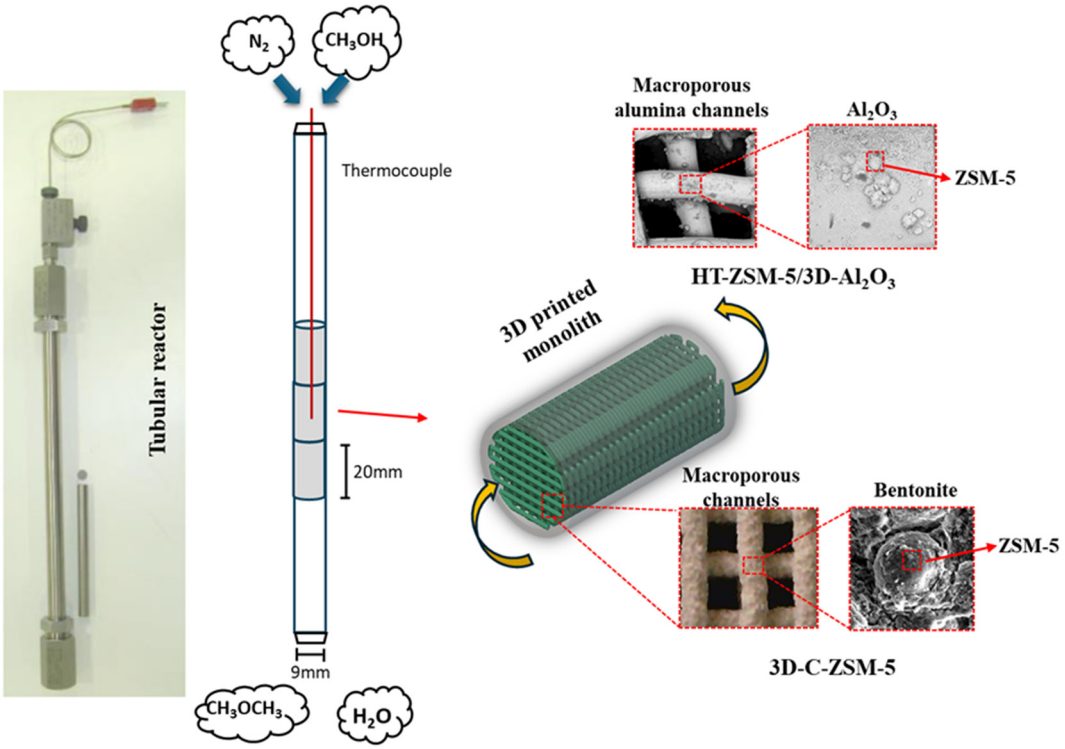

Fig. 13 Schematic representation of monoliths dimensions and employed reactor.

The activity of the two 3D-printed ZSM-5-containing monoliths and that of the corresponding ZSM-5 powders are presented as a function of temperature and space velocity in Fig. 14a and b, respectively. The figures also include the equilibrium methanol conversion dictated by thermodynamics for the specific temperature/pressure conditions, calculated by AspenPlus with the use of an RGibbs reactor model and the Peng–Robinson equation of state. The 3D-printed zeolites exhibit very good activity, with conversion ranging between 20–45% at 225 °C and increasing to values close to equilibrium (~85%) at 275 °C and WHSV 51–55 h^{-1}. Lower space velocities lead, as expected, to higher conversion. At the lowest WHSV examined and 275 °C, thermodynamic equilibrium is reached by both the structured catalysts and their powder counterparts.

Comparing the preparation strategies followed for the additive manufacturing of the catalysts, the monolith prepared by growing ZSM-5 crystallites on the 3D-printed α-Al_2O_3 structure (HT-ZSM-5/3D-Al_2O_3) achieves the highest performance when compared on ZSM-5 weight basis. Its activity outperforms that of the monolith prepared by 3D printing a mixture of crystalline ZSM-5 with bentonite (3D-C-ZSM-5), achieving over double conversion at 225 °C. It is also interesting to note that whereas the 3D-C-ZSM-5 monolith presents lower activity than the commercial crystalline ZSM-5 powder, the HT-ZSM-5/3D-Al_2O_3 monolith's performance surpasses that of the corresponding hydrothermally prepared ZSM-5 powder. While variations in bed volume between powders and monoliths may alter reactor flow dynamics and influence catalytic performance, the underlying trends remain consistent over a broad range of temperatures and space velocities.

Based on these observations, it appears that the growth of ZSM-5 crystallites directly on the α-Al_2O_3 substrate leads to better dispersion of the active sites on the 3D-printed monolithic structure, rendering more acid sites available for surface catalysis. This is supported by the SEM-EDX analysis (see Fig. 7 and 8), which visually confirms the formation of ZSM-5 nano-crystallites on α-Al_2O_3. Moreover, its improved activity compared to its powder counterpart (when compared on equal ZSM-5 content) reinforces this argument and demonstrates that the 3D-printed α-Al_2O_3 support provides a unique substrate for the growth of surface ZSM-5 nano-crystallites. It should be noted that acid site accessibility is inferred indirectly from dry pyridine-FTIR normalization, SEM-EDX dispersion, and catalytic performance trends and has not been verified under wet conditions. On the contrary, in the case of the direct 3D printing of crystalline ZSM-5 in a mixture with bentonite, it is possible that a fraction of the ZSM-5 particles are embedded in the bentonite matrix and may therefore exhibit reduced accessibility with the reacting methanol molecules. This, in combination with the alkali cations in bentonite that neutralize some of the acid sites, explains its worse performance in the methanol-to-DME dehydration reaction in comparison with both the HT-ZSM-5/3D-Al_2O_3 monolith and its crystalline ZSM-5 powder counterpart. It should however be noted that this comparison is conducted on ZSM-5 basis and not on total catalyst weight

This journal is © The Royal Society of Chemistry 2026

Open Access Article. Published on 12 February 2026. Downloaded on 4/29/2026 9:04:27 PM.
This article is licensed under a Creative Commons Attribution 3.0 Unported Licence.

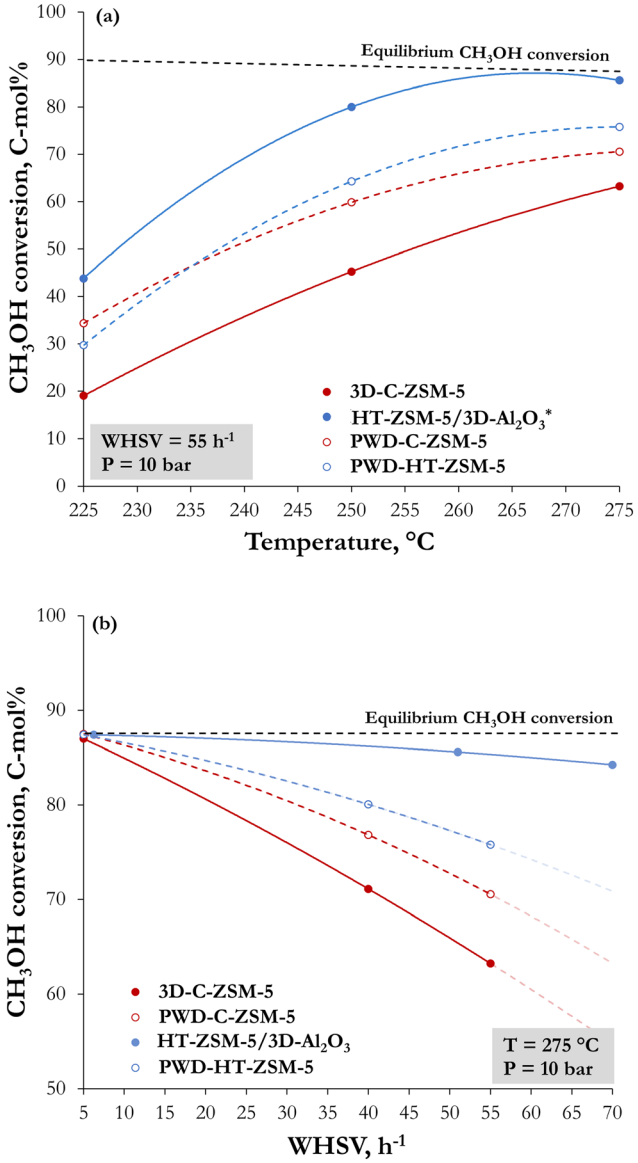

Fig. 14 Methanol conversion as a function of (a) temperature and (b) WHSV for the ZSM-5-containing 3D-printed monoliths and corresponding powders (*experiment performed at WHSV = 51 h^{-1}).

or volume. This inevitably favors the HT-ZSM-5/3D-Al_2O_3 monolith, which consists of highly dispersed ZSM-5 particles on the α-Al_2O_3 structure. In industrial applications, the total catalyst mass/reactor volume are important cost-relevant parameters that should also be considered.

Comparison with literature proved to be difficult considering that, to the best of our knowledge, only three studies[35–37] report the preparation and evaluation of ZSM-5-based 3D-printed catalysts in the methanol-to-DME reaction. Lefevere *et al.*[35] report equilibrium methanol conversion and >99.5% DME selectivity over ZSM-5-coated stainless steel 3D-printed supports at 250 °C, 1 bar and WHSV 4.56 h^{-1}. In the studies by the group of Rownaghi,[36,37] methanol conversion between 70–93% is reported at atmospheric pressure, temperature range 180–400 °C and WHSV ~3 h^{-1} (calc. on ZSM-5 basis), over direct 3D-printed monoliths containing ~85 wt% H-ZSM-5 and bentonite as binder. At the experimental conditions employed in literature, methanol conversion is close to equilibrium therefore benchmarking of the materials reported herein cannot be safely performed.

Table 3 Carbon content measured *via* elemental analysis after use in the methanol-to-DME reaction at temperatures 225–275 °C and WHSV 55 h^{-1}

	C, wt%	
Used sample	On material basis	On ZSM-5 basis
3D-C-ZSM-5	0.44	0.74
HT-ZSM-5/3D-Al_2O_3[a]	0.08	2.00
PWD-C-ZSM-5	6.85	6.85
PWD-HT-ZSM-5	1.10	1.10

[a] Experiment performed at WHSV 51 h^{-1}.

One of the major drawbacks in zeolite use for methanol conversion to DME is coke formation, which constitutes the main cause of catalyst deactivation.[54–56] Although catalyst deactivation was not systematically assessed with long-term stability tests, the carbon content of the samples after testing in the methanol dehydration reaction at temperatures 225–275 °C and WHSV 51–55 h^{-1} was determined by elemental analysis. The amount of carbonaceous deposits is presented in Table 3, expressed both on total material and on ZSM-5 basis to allow fair comparison across catalyst forms. A substantial amount of coke deposits is accumulated only on the surface of the commercial crystalline ZSM-5 powder, much higher than that formed on the hydrothermally synthesized ZSM-5 powder, despite the higher activity of the latter. This can be linked to its lower SiO_2/Al_2O_3 ratio, and thus higher number of strong Brønsted acid sites as measured by FTIR-pyridine (see Fig. 5 and 12) that catalyze the conversion of methanol to olefins, which react further to coke species. This observation is also consistent with the small amount of olefin by-products detected in the reaction products of both the ZSM-5 powders. The 3D-printed monolithic structures demonstrate low carbon deposition. Even when these values are normalized to the ZSM-5 content of each material, the coking tendency remains low. This holds true especially for the HT-ZSM-5/3D-Al_2O_3 monolith, considering its very high activity, and underlines the beneficial role of the well-defined architecture in improving the dispersion of the active acid sites.

4. Conclusions

This study reports the successful preparation of 3D-printed highly active and selective ZSM-5-containing structures of woodpile configuration for the dehydration of methanol to DME. Robocasting was effectively utilized for the preparation of a α-alumina structured support with remarkable mechanical strength. ZSM-5 nano-crystallites were then successfully synthesized hydrothermally on its surface, with the α-alumina 3D-printed monolith acting essentially as the

Open Access Article. Published on 12 February 2026. Downloaded on 4/29/2026 9:04:27 PM.
This article is licensed under a Creative Commons Attribution 3.0 Unported Licence.

initial seed for the growth of the MFI zeolitic framework. Based on Rietveld refinement of the diffraction pattern of the ZSM-5/α-Al_2O_3 monolith and its textural properties, the ZSM-5 loading was estimated to be in the range of ~4 wt%. When compared on an equivalent ZSM-5 basis with a 3D-printed monolithic structure of the same configuration prepared *via* direct 3D printing of a mixture of commercial crystalline ZSM-5 and bentonite as binder, the ZSM-5/α-Al_2O_3 catalyst exhibits up to twice the activity in methanol conversion with 100 C-mol% DME selectivity. Moreover, its performance outperforms that of the corresponding hydrothermally prepared ZSM-5 powder, as opposed to the direct 3D-printed monolith that is less active than the commercial ZSM-5 used for its preparation.

Based on SEM-EDX findings, this behavior is attributed to the excellent dispersion of the ZSM-5 active sites on the 3D-printed α-Al_2O_3 structure, which provides a unique substrate for the growth of surface ZSM-5 nano-crystallites. Despite its good performance, future efforts should focus on increasing the ZSM-5 loading to address issues related to large reactor volume requirements that are very important for industrial implementation. This can be achieved by optimizing the ZSM-5 hydrothermal synthesis parameters, employing hierarchical porous α-Al_2O_3 ceramic structures with internal microporosity as support, *etc.* In parallel, additional optimization of the monolith fabricated by direct 3D printing of ZSM-5 and bentonite may be pursued through increased zeolite loading, optimized printing density, and the evaluation of alternative binders. Overall, this work demonstrates that 3D printing can be successfully employed to fabricate structured materials, suitable for use in catalytic applications, with high catalytic performance and high mechanical strength.

Author contributions

Vasiliki Koidi: writing – original draft, writing – review & editing, investigation, visualization. Savvas Koltsakidis: writing – original draft, investigation, visualization. Stamatia Karakoulia: investigation. Dimitrios Tzetzis: conceptualization, methodology, supervision, writing – review & editing. Angelos A. Lappas: writing – review & editing, validation, supervision. Eleni Heracleous: writing – review & editing, writing – original draft, conceptualization, methodology, supervision, funding acquisition.

Conflicts of interest

There are no conflicts to declare.

Data availability

Supplementary information (SI) is provided, presenting in detail the calculation of mass/heat transfer criteria. All other data will be made available on request.

Supplementary information is available. See DOI: https://doi.org/10.1039/d6re00015k.

Acknowledgements

This research was supported by the Hellenic Foundation for Research and Innovation (H.F.R.I.) in the framework of the action "1st Call for H.F.R.I. Research Projects to Support Faculty Members & Researchers and Procure High-Value Research Equipment" (Project Number: HFRI-FM17-62).

References

1 G. A. Olah, A. Goeppert and G. K. S. Prakash, *J. Org. Chem.*, 2009, **74**, 487–498.
2 M. Müller and U. Hübsch, in *Ullmann's Encycl. Ind. Chem.*, Wiley-VCH Verlag GmbH & Co. KGaA, Weinheim, 2012, pp. 305–308.
3 C. Arcoumanis, C. Bae, R. Crookes and E. Kinoshita, *Fuel*, 2008, **87**, 1014–1030.
4 Z. Lei, Z. Zou, C. Dai, Q. Li and B. Chen, *Chem. Eng. Sci.*, 2011, **66**, 3195–3203.
5 P. Cheung, A. Bhan, G. J. Sunley and E. Iglesia, *Angew. Chem., Int. Ed.*, 2006, **45**, 1617–1620.
6 P. Cheung, E. Iglesia, J. G. Sunley, D. J. Law and A. Bhan, US7465822, 2006.
7 I. A. Bakare, O. Muraza, M. A. Sanhoob, K. Miyake, Y. Hirota, Z. H. Yamani and N. Nishiyama, *Fuel*, 2018, **211**, 18–26.
8 J. Ereña, I. Sierra, A. T. Aguayo, A. Ateka, M. Olazar and J. Bilbao, *Chem. Eng. J.*, 2011, **174**, 660–667.
9 A. A. Rownaghi, F. Rezaei, M. Stante and J. Hedlund, *Appl. Catal., B*, 2012, **119–120**, 56–61.
10 H. J. Chen, C. W. Fan and C. S. Yu, *Appl. Energy*, 2013, **101**, 449–456.
11 T. Ogawa, N. Inoue, T. Shikada and Y. Ohno, *J. Nat. Gas Chem.*, 2003, **12**, 219–227.
12 K. C. Tokay, T. Dogu and G. Dogu, *Chem. Eng. J.*, 2012, **184**, 278–285.
13 W. H. Chen, B. J. Lin, H. M. Lee and M. H. Huang, *Appl. Energy*, 2012, **98**, 92–101.
14 F. Raoof, M. Taghizadeh, A. Eliassi and F. Yaripour, *Fuel*, 2008, **87**, 2967–2971.
15 F. Hayer, H. Bakhtiary-Davijany, R. Myrstad, A. Holmen, P. Pfeifer and H. J. Venvik, *Chem. Eng. Process.*, 2013, **70**, 77–85.
16 T. A. Semelsberger, R. L. Borup and H. L. Greene, *J. Power Sources*, 2006, **156**(2), 497–511.
17 I. H. Kim, S. Kim, W. Cho and E. S. Yoon, *Comput.-Aided Chem. Eng.*, 2010, **28**, 799–804.
18 Z. Azizi, M. Rezaeimanesh, T. Tohidian and M. R. Rahimpour, *Chem. Eng. Process.*, 2014, **82**, 150–172.
19 E. Catizzone, C. Freda, G. Braccio, F. Frusteri and G. Bonura, *J. Energy Chem.*, 2021, **58**, 55–77.
20 E. Catizzone, G. Bonura, M. Migliori, F. Frusteri and G. Giordano, *Molecules*, 2018, **23**, 31.
21 V. Vishwanathan, K. W. Jun, J. W. Kim and H. S. Roh, *Appl. Catal., A*, 2004, **276**, 251–255.
22 V. Dieterich, A. Buttler, A. Hanel, H. Spliethoff and S. Fendt, *Energy Environ. Sci.*, 2020, **13**, 3207–3252.

 This journal is © The Royal Society of Chemistry 2026

Open Access Article. Published on 12 February 2026. Downloaded on 4/29/2026 9:04:27 PM. This article is licensed under a Creative Commons Attribution 3.0 Unported Licence.

23 A. Cybulski and J. Moulin, *Catal. Rev.: Sci. Eng.*, 1994, **36**, 179–270.
24 L. Chatre, J. Socci, S. J. Adams, P. Denissenko and N. Cherkasov, *Chem. Eng. J.*, 2021, **420**, 129762.
25 C. J. C. Nocheseda, F. P. Liza, A. K. M. Collera, E. B. Caldona and R. C. Advincula, *Addit. Manuf.*, 2021, **48**, 102380.
26 J. Lee, S. Choo, H. Ju, J. Hong, S. E. Yang, F. Kim, D. H. Gu, J. Jang, G. Kim, S. Ahn, J. E. Lee, S. Y. Kim, H. G. Chae and J. S. Son, *Adv. Energy Mater.*, 2021, **11**, 2100190.
27 W. Kang, L. Zeng, S. Ling, R. Yuan and C. Zhang, *Energy Storage Mater.*, 2021, **35**, 345–352.
28 L. Chen, S. Zhou, M. Li, F. Mo, S. Yu and J. Wei, *Catalysts*, 2022, **12**, 1081.
29 X. Zhou and C. J. Liu, *Adv. Funct. Mater.*, 2017, **27**, 1701134.
30 C. Parra-Cabrera, C. Achille, S. Kuhn and R. Ameloot, *Chem. Soc. Rev.*, 2018, **47**, 209–230.
31 E. Bogdan and P. Michorczyk, *Materials*, 2020, **13**, 4534.
32 S. Lawson, X. Li, H. Thakkar, A. A. Rownaghi and F. Rezaei, *Chem. Rev.*, 2021, **121**, 6246–6291.
33 J. Chen, P. Wu, F. Bu, Y. Gao, X. Liu and C. Guan, *DeCarbon*, 2023, **2**, 100019.
34 J. Zhu, P. Wu, Y. Chao, J. Yu, W. Zhu, Z. Liu and C. Xu, *Chem. Eng. J.*, 2022, **433**, 13434.
35 J. Lefevere, M. Gysen, S. Mullens, V. Meynen and J. Van Noyen, *Catal. Today*, 2013, **216**, 18–23.
36 F. Magzoub, X. Li, S. Lawson, F. Rezaei and A. A. Rownaghi, *Fuel*, 2020, **280**, 118628.
37 F. Magzoub, S. Lawson, F. Rezaei and A. A. Rownaghi, *Energy Fuels*, 2021, **35**, 2619–2629.
38 G. Bonura, S. Todaro, V. Middelkoop, Y. de Vos, H. C. L. Abbenhuis, G. Gerritsen, A. J. J. Koekkoek, C. Cannilla and F. Frusteri, *J. CO_2 Util.*, 2023, **70**, 102458.
39 S. Koltsakidis, V. Koidi, A. Lappas, E. Heracleous and D. Tzetzis, *Int. J. Adv. Des. Manuf. Technol.*, 2023, **126**, 259–271.
40 W. Schmidt, U. Wilczok, C. Weidenthaler, O. Medenbach, R. Goddard, G. Buth and A. Cepak, *J. Phys. Chem. B*, 2007, **111**, 13538–13543.
41 C. A. Emeis, *J. Catal.*, 1993, **141**, 347–354.
42 K. S. W. Sing, D. H. Everett, R. A. W. Haul, L. Moscou, R. A. Pierotti, J. Rouquerol and T. Siemeniewska, *Pure Appl. Chem.*, 1985, **57**, 603–619.
43 J. C. Groen, L. A. A. Peffer, J. A. Moulijn and J. Pérez-Ramírez, *Chem. – Eur. J.*, 2005, **11**, 4983–4994.
44 P. L. Llewellyn, J. P. Coulomb, Y. Grillet, J. Patarin, G. Andre and J. Rouquerol, *Langmuir*, 1993, **9**, 1852–1856.
45 J. Lefevere, L. Protasova, S. Mullens and V. Meynen, *Mater. Des.*, 2017, **134**, 331–341.
46 N. Y. Topsøe, K. Pedersen and E. G. Derouane, *J. Catal.*, 1981, **70**, 41–52.
47 J. Lefevere, S. Mullens and V. Meynen, *Chem. Eng. J.*, 2018, **349**, 260–268.
48 R. B. Borade, A. Adnot and S. Kaliaguine, *Zeolites*, 1992, **12**, 76–80.
49 T. Baba, Y. Inoue and Y. Ono, *J. Catal.*, 1996, **159**, 230–235.
50 E. V. Makshina, J. Canadell, J. van Krieken and B. F. Sels, *ACS Sustainable Chem. Eng.*, 2022, **10**, 6196–6204.
51 S. R. Batool, V. L. Sushkevich and J. A. van Bokhoven, *ACS Catal.*, 2024, **14**, 678–690.
52 D. Masih, S. Rohani, J. N. Kondo and T. Tatsumi, *Appl. Catal., B*, 2017, **217**, 247–255.
53 Y. Fu, T. Hong, J. Chen, A. Auroux and J. Shen, *Thermochim. Acta*, 2005, **434**, 22–26.
54 H. An, F. Zhang, Z. Guan, X. Liu, F. Fan and C. Li, *ACS Catal.*, 2018, **8**, 9207–9215.
55 G. Laugel, X. Nitsch, F. Ocampo and B. Louis, *Appl. Catal., A*, 2011, **402**, 139–145.
56 H. Schulz, *Catal. Today*, 2010, **154**, 183–194.